Insight into hydrothermal aging effect on Pd sites over Pd/LTA and Pd/SSZ-13 as PNA and CO oxidation monolith catalysts

(article starts on next page)

Insight into hydrothermal aging effect on Pd sites over Pd/LTA and Pd/SSZ-13 as PNA and CO oxidation monolith catalysts

Aiyong Wang[a], Kristina Lindgren[b], Mengqiao Di[c], Diana Bernin[a], Per-Anders Carlsson[c], Mattias Thuvander[b], Louise Olsson[a],*

[a] *Competence Centre for Catalysis, Chemical Engineering, Chalmers University of Technology, Gothenburg, SE 412 96, Sweden*
[b] *Department of Physics, Chalmers University of Technology, Gothenburg, SE 412 96, Sweden*
[c] *Competence Centre for Catalysis, Applied Chemistry, Chalmers University of Technology, Gothenburg, SE 412 96, Sweden*

ARTICLE INFO

ABSTRACT

In this study, Pd/LTA and Pd/SSZ-13 were prepared and then hydrothermally aged at the temperature of 750, 800, 850, and 900 °C. Multiple Pd species, including isolated Pd ions (Pd^{2+} and $[Pd(OH)]^+$) and $1 \sim 2$ nm PdO_x nanoparticles, were presented in two fresh samples. The Pd/LTA sample showed remarkable hydrothermal stability, but the Pd/SSZ-13 sample experienced severe damage after aging at 900 °C. The destruction of the aged Pd/SSZ-13 sample led to the migration and sintering of PdO_x nanoparticles, which formed bulk PdO_x particles on the surface of the zeolite crystallite. A large number of PdO_x nanoparticles were retained after aging of the Pd/LTA sample. Pd/LTA contained a higher concentration of Pd^{2+} sites, while Pd/SSZ-13 had more $[Pd(OH)]^+$ sites. It is found that the improvement of NO adsorption ability with CO addition onto Pd^{2+} was more significant than onto $[Pd(OH)]^+$.

1. Introduction

Nitrogen oxides (NO_x) in the exhausts from lean-burn engines (i.e., gasoline and diesel), entail significant challenges for the aftertreatment society [1]. The NO_x must be removed due to the serious environmental issues caused by NO_x, e.g., acid rain, smog, and ozone depletion. Fortunately, the application of ammonia selective catalytic reduction (NH_3-SCR) greatly reduces NO_x emissions from vehicles using representative catalyst systems, such as Cu/zeolites [2] and V_2O_5-WO_3/TiO_2 [3].

As environmental regulations have become more stringent in recent years, the cold start issue has received increasing attention in the catalysis field [4,5]. The traditional SCR catalyst has relatively large operating temperature window (e.g., $200 \sim 400$ °C) [6,7]. One of the main reasons for this is that the ammonia is supplied through a urea solution and urea cannot be dosed below 200 °C, since at low temperature deposits form, such as biuret and cyanuric acid [8]. Therefore, one possible approach is to employ a material that can adsorb NO_x (mainly in the form of NO) at a low temperature (below urea dosing temperature) and to desorb it at a high temperature, e.g., $200 - 400$ °C. This material is called a passive NO_x adsorber (PNA) catalyst [9,10]. Using PNA and SCR components simultaneously in the aftertreatment system, where

PNA is located before or as dual-layer with an SCR catalyst in the monolith [9], can greatly help to solve the cold-start challenge of NO_x emissions.

Supported Pd zeolites are one of the most attractive kinds of materials for the PNA catalyst. Pd zeolites have been studied using various framework topologies such as ZSM-5, BEA, and SSZ-13 [11,12]. The effect of zeolite support on NO_x adsorption/desorption efficiency has been systematically investigated [10,13]. One recent study suggested [10] that Pd supported on small-pore zeolites, such as SSZ-13, resulted in a relatively high desorption temperature of NO_x. This has been further confirmed by recent research [9,14]. Lee and coworkers [11] and Zheng et al. [13] have found two types of Pd sites able to adsorb NO at a low temperature ($\sim$ 100 °C). These active Pd species are isolated Pd(II) ions and small PdO_x species. It has also been found that short-term moderate hydrothermal treatment (e.g., 750 °C for 2 h) can increase the NO_x storage capacity of Pd/zeolites since more isolated Pd^{2+} ions are formed [9,15]. The presence of CO has two distinct effects on the performance for NO_x storage: one positive [16] and one negative [17,18]. The positive effect is an increased adsorption amount of NO_x and higher desorption temperatures after adding CO. The negative effect is that the feeding of CO can deactivate Pd/zeolites during repeated adsorption/desorption cycles. This is mainly because of the loss of

---

* Corresponding author.
E-mail address: louise.olsson@chalmers.se (L. Olsson).

isolated Pd(II) ions and the formation of bulk PdO_x particles [17].

An LTA (Linde type A) zeolite with high Si/Al ratio (> 10) was recently successfully synthesized [19]. The remarkable stability of a Cu/LTA catalyst for NH_3-SCR reaction has been recently investigated by Ryu et al. and our group [20,21]. For example, minor structure and activity changes were found after hydrothermal aging at 900 °C. Given the impressive hydrothermal stability of the Cu/LTA catalyst for NH_3-SCR reaction, it is possible that a Pd/LTA catalyst might also achieve the promising stability needed for the PNA application. Lim et al. [22] have studied Pd-supported LTA catalysts for the application of CH_4 oxidation, which is the only work that can be found using a Pd/LTA catalyst. However, to our knowledge, there are no published papers that employ the LTA zeolite as a Pd support for a PNA catalyst.

One key factor of automotive catalysts is the long-term hydrothermal stability due to the occasional regenerations of a diesel particulate filter at harsh temperatures. The objective of this study is to gain insight into the performance and the hydrothermal stability of a Pd/LTA catalyst as a potential PNA material. For comparison, a Pd/SSZ-13 catalyst with similar components, e.g., Pd loading and Si/Al ratio, was also prepared and studied. The two samples, Pd/LTA and Pd/SSZ-13, before and after aging, were used for different reactions, including CO oxidation and NO-TPD with and without CO. To identify catalyst functions and to understand the changes in depth in the nature of the structure and Pd species upon aging, the materials were further characterized using multiple techniques. The techniques included ICP, BET, XRD, ^{27}Al ss-NMR, APT, TEM, HAADF-STEM, *in situ* DRIFTS, NH_3-TPD, and O_2-TPD.

2. Experimental section

2.1. Catalyst synthesis

SSZ-13 and LTA materials with Si/Al close to 15 were prepared using methods reported in the literature [21,23]. Pd was loaded into SSZ-13 and LTA zeolites with the incipient wetness impregnation approach with a $Pd(NO_3)_2$ solution. The details were reported in the recent publication [21]. Briefly, the $Pd(NO_3)_2$ solution was diluted with MilliQ water and then added into the powder of H/LTA or H/SSZ-13 with continuous manual stirring. After adding $Pd(NO_3)_2$, the resulting powder was further mixed with a metal spoon for 15 min. until a homogenous light yellow color was obtained. Thereafter, the sample was dried in an oven of 60 °C. The obtained powder was further manually ground and then calcined at 600 °C for 120 min. with a heating ramp of 2 °C/min in the furnace with static air.

Finally, palladium-loaded powder was applied for the monolithic washcoating with a cell density of 400 cpsi. The size of the monolith was around 15 mm in diameter and 20 mm in length. Disperal P2 from Sasol was added to the powder with binder function to increase the adhesion of the zeolite. The ratio between zeolite powder and binder was controlled to be around 95 to 5. The slurry used for the washcoat consisted of around 20 % solid and 80 % liquid in weight, where the liquid consisted of 50 % MilliQ water and 50 % ethanol in weight. The entire weight of washcoat on the monolith was around 300 mg for all the samples, with a difference of no more than 5 mg. The obtained monolith was further calcined at 500 °C for 120 min with a heating ramp of 5 °C/min in the furnace with static air. Fresh samples directly from the furnace are named as Pd/zeolite_fresh (zeolite = LTA or SSZ-13). Then, the monolith was pre-treated at 750 °C for 2 h with 5 % H_2O, 10 % O_2 balanced in Ar in a flow reactor and named as Pd/zeolite_750 (zeolite = LTA or SSZ-13). This step was added to improve the ion exchange level of Pd ions in the zeolite [9]. The monolith was further aged at 800/850 °C for 15 h and also treated at 900 °C for 8 h with 5 % H_2O, 10 % O_2 balanced in Ar. The obtained samples are named as Pd/zeolite_800, Pd/zeolite_850, and Pd/zeolite_900 (zeolite = LTA or SSZ-13), respectively.

2.2. Catalyst characterization

Inductively Coupled Plasma (ICP) used for the elemental analysis was performed by ALS Scandinavia AB. The instrument model of Tristar 3000 from Micromeritics was applied for the measurement of N_2 adsorption-desorption isotherms at the temperature of 77 K. Prior to the test, the sample was degassed at 200 °C overnight with continuous flowing N_2. The specific surface areas were obtained based on Brunauer-Emmett-Teller (BET) method and pore volumes were acquired with the t-plot method.

Powder X-Ray Diffraction (XRD) analysis were performed with the instrument model of SIEMENS diffractometer D5000. The setup was conducted at 40 mA and 40 kV with an X-ray energy of Copper K-α radiation ($\lambda = 1.5418$ Å). The spectra were collected from 5 to 40 degree of 2 theta with 0.02° per step.

Solid-state NMR analysis of ^{27}Al was performed on an Agilent Inova 600 MHz instrument using a 3.2 mm HX (double resonance) magic-angle spinning (MAS) probe. Analysis was documented at a rate of 15 kHz. 1 M $Al(NO_3)_3$ solution was used as the reference for the ^{27}Al ppm scale. The repetition delay used was 3 s, and the excitation was performed using a 10° radio frequency (RF) pulse, which was calibrated on the reference solution. The ^{27}Al NMR spectra were collected 512 times and then accumulated. After that, the signal was normalized by the weight of catalyst used for analysis.

The tips for Atom Probe Tomography (APT) were prepared using a FEI Versa 3D Focused Ion Beam/Scanning Electron Microscope (FIB/SEM). The 4 μm diameter of the particles were too small for a standard lift out, and thus a few particles were lift out together, held by Pt deposition, and attached to an Si post on a wafer. The details are described in Supplementary Information (Fig. S-1). The APT analysis was performed in a LEAP 3000X HR (Imago Scientific Instruments) with a reflectron and a 532 nm wavelength laser. Due to the high risk of premature fracture, the temperature was kept relatively high at 70 K and the laser energy was 0.7 nJ, which is also relatively high. The laser pulse frequency was 200 kHz, and the detection rate was 0.2 %. Reconstruction and data analysis were done using the IVAS 3.6.14 software (Cameca).

Transmission Electron Microscopy (TEM) images were acquired to observe the tomography of the catalysts at different magnifications with an FEI Tecnai T20 instrument conducted at 200 kV using a LaB_6 filament. The samples were primarily dispersed in ethanol and followed by ultrasonication. One drop of the resultant solid-liquid mixture was loaded on a copper grid (3 mm) covered by a porous carbon film. The nature of Pd species were further studied with Scanning Transmission Electron Microscopy (STEM) using a FEI Titan 80–300 with a high-angle annular dark-field (HAADF) detector. The instrument was carried out in the STEM mode with an operating voltage of 300 kV.

NH_3 Temperature-Programmed Desorption (NH_3-TPD) was conducted with the same flow reactor system as the NH_3-SCR experiments, as described in Section 2.3. The procedure was as follows: (1) pre-treat the monolith at 500 °C in O_2/Ar with 5 % H_2O for 30 min; (2) cool the monolith to 100 °C in Ar with 5 % H_2O; (3) adsorb 400 ppm NH_3 in Ar with 5 % H_2O for 1 h; (4) purge the monolith in Ar with 5 % H_2O for 20 min at 100 °C; and (5) heat the monolith from 100 to 650 °C at 20 °C/min in Ar with 5 % H_2O.

O_2 Temperature-Programmed Desorption (O_2-TPD) was conducted using a Differential Scanning Calorimeter with a mass spectrometer (MS) as detector. The catalyst was pre-treated at 150 °C for 60 min with 5% O_2 in Ar and cooled to 25 °C and maintained for 30 min in O_2/Ar. After that, the catalyst was flushed with Ar for 30 min. TPD was then conducted from 25 to 800 °C using a rate of 10 °C/min in Ar.

In situ Diffuse Reflectance Infrared Fourier Transform Spectroscopy (DRIFTS) was performed using a Bruker Vertex 70 spectrometer. The instrument is fitted with an MCT detector. The spectra were acquired with 256 scans and a resolution of 4 cm^{-1}. The catalyst was first pretreated in 10 % O_2/Ar for 60 min at 500 °C and cooled to 80 °C in the

same flow. Background was then taken at 80 °C before NO adsorption. After that, 200 ppm NO was added into the gas phase for 30 min of adsorption. Using the obtained background, the spectrum was continuously recorded every minute.

2.3. Flow reactor tests

CO oxidation experiments was performed on the monolith using 500 ppm CO, 5 % H_2O, 8 % O_2 in Ar with the flow rate of 1200 mL/min. The monolith was first heated to 300 °C and maintained for 60 min, and then cooled to 80 °C at a ramp rate of 20 °C/min and maintained at each step for 60 min (20 °C per step).

For NO-TPD experiments with or without CO, the monolith was subjected to 200 ppm NO, 200 ppm CO (if used), 8 % O_2, 5 % H_2O in Ar with the flow rate of 350 mL/min at the temperature of 80 °C for 60 min to saturate the PNA. Thereafter, the monolith was first purged with 8 % O_2, 5 % H_2O in Ar for 30 min at 80 °C and heated up to 500 °C at a ramp rate of 20 °C/min. Note that, before the TPD experiments, the monolith was pre-treated using 8 % O_2, 5 % H_2O in Ar for 20 min at 500 °C.

3. Results and discussion

3.1. Characterizations

3.1.1. Textural properties of Pd/zeolites (XRD, BET, ^{27}Al ss-NMR)

As presented in Table 1, two samples with comparable Si to Al ratios (~15) and Pd loadings (~1.5 wt.%) for each zeolite were prepared. The Pd/Al ratios were controlled to be approximately 0.2. Note that the scope of this work is not only to elucidate the performance of Pd/zeolites, i.e., LTA and SSZ-13, for a PNA application, but to understand the evolution of different Pd species after harsh aging. Considering the Si/Al and Pd/Al ratios and referencing the literature [11,13], the samples prepared in the study were to consist of not only isolated Pd(II) ions but also PdO$_x$ nanoparticles. This was further investigated with different characterization methods, e.g., TEM.

Table 1 shows specific surface areas and pore volumes for both fresh and aged samples. Only minor changes were found for the Pd/LTA sample upon aging compared to the Pd/SSZ-13 sample. For example, the loss of surface areas at aging up to 900 °C for Pd/LTA and Pd/SSZ-13 were around 12 % and 43 %, which was similar to findings for the pore volumes of the samples. This suggests that the Pd/LTA sample showed remarkable hydrothermal stability, similar to the Cu/LTA sample reported previously [20,21]. However, the structure of the Pd/SSZ-13 sample experienced severe damage after the harsh aging at 900 °C.

The lower panel of Fig. 1 presents the X-ray diffraction patterns for the fresh (solid black line) and 900 °C aged (dotted red line) Pd/LTA samples. Both samples show diffraction peaks essentially identical to the parent H/LTA [21]. No significant intensity decline was found after 900 °C aged, demonstrating the robust stability of LTA zeolite topology
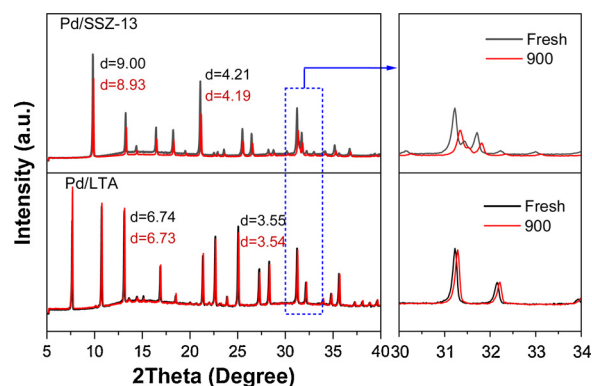

Fig. 1. XRD patterns for the fresh and 900 °C aged Pd/LTA (lower panels) and Pd/SSZ-13 (upper panels) samples.

[20] and XRD is not sensitive to small structural changes. In contrast, XRD patterns displayed noticeable variation in the Pd/SSZ-13 samples, presented in the upper panel of Fig. 1, before and after hydrothermal aging. In other words, a significant signal drop was observed due to the decreased crystallinity of the SSZ-13 structure upon aging at 900 °C, in line with the BET results (Table 1).

As highlighted in the enlarged right panels of Fig. 1, the zeolite diffraction peaks shifted to higher angles in the aged sample than those in the fresh state, which is surely a result of change in the zeolite lattice parameter [24]. According to the Bragg equation ($d = \frac{n\lambda}{2sin\theta}$), the d-spacing related to the two strong peaks in Pd/zeolite was calculated, and the obtained values were inserted into the figure. The value of d-spacing reduced from 9.00–8.93 Å in the 900 °C aged Pd/SSZ-13 sample, which suggests lattice contractions [24]. However, the change in d-spacing was not apparent for the aged Pd/LTA sample. Su et al. [25] reported a novel Pd-doped CeO_2 structure, where Pd adopted a square planar configuration, not the expected octahedral configuration. However, this was not the case in Pd/LTA or Pd/SSZ-13 catalyst. Considering the much larger size of Pd ion in comparison of Al or Si, if Pd was doped into the zeolite framework, it would inevitably cause expansion of zeolite structure and even the destruction of the framework structure. But, as shown in Fig. 1 of XRD results, no structure expansion was found after 900 °C aging for both samples.

^{27}Al solid-state NMR (^{27}Al ss-NMR) was demonstrated to be more sensitive than XRD for disclosing the local changes of zeolite frameworks upon hydrothermal aging [26]. Thus, this technique was used to further investigate the influence of aging on the local Al environment to more precisely determine zeolite structural changes [27,28]. Fig. 2 shows ^{27}Al ss-NMR spectra for the degreened (750 °C) and aged (900 °C) Pd/LTA and Pd/SSZ-13 samples. All spectra exhibited resonances at approximately 59 and 0 ppm, arised from tetrahedrally coordinated framework aluminum (Al$_F$) and extra-framework aluminum (Al$_{EF}$), respectively [29,30]. After aging at 900 °C, both Pd/LTA and Pd/SSZ-13 samples showed a decline in Al$_F$ (i.e., 59 ppm) intensity due to dealumination as compared to their degreened counterparts. To acquire the quantitative degree of dealumination during the aging process, the Al$_F$ signals were integrated, normalized using the weight of samples, thereafter, a ratio with the relevant 750 °C aged Pd/zeolite Al$_F$ signals was determined. The obtained values of Al$_F$(900)/Al$_F$(750) have been inserted into Fig. 2, where the values are 0.95 and 0.71 for Pd/LTA and Pd/SSZ-13. Accordingly, the Pd/SSZ-13 sample experienced more significant intensity loss than the Pd/LTA sample, indicative of a difference in stability between the two samples. Overall, according to BET, XRD and ^{27}Al ss-NMR results, it was found that the framework structures and crystallinity of the Pd/SSZ-13 sample underwent significant changes upon aging at 900 °C, while only minor changes were found for the Pd/LTA sample.
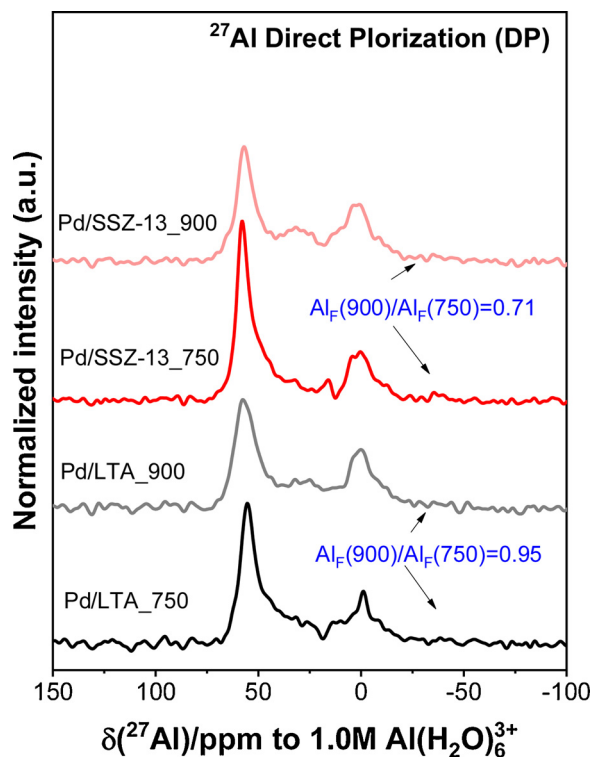
Table 1
ICP results, BET surface areas (S$_{BET}$), and pore volumes (V$_{pore}$) using t-plot method for fresh and aged Pd/LTA and Pd/SSZ-13 samples.

Sample	Pd content (wt. %)	Si/Al ratio	Pd/Al ratio	S$_{BET}$ (m^2 g^{-1})	V$_{pore}$ (cm^3 g^{-1})
Pd/LTA_fresh	1.4	14.5	0.15	554	0.30
Pd/LTA_750	–	–	–	547	0.29
Pd/LTA_800	–	–	–	542	0.28
Pd/LTA_850	–	–	–	511	0.27
Pd/LTA_900	–	–	–	487	0.25
Pd/SSZ-13_fresh	1.6	15.0	0.18	563	0.29
Pd/SSZ-13_750	–	–	–	551	0.28
Pd/SSZ-13_800	–	–	–	520	0.27
Pd/SSZ-13_850	–	–	–	433	0.20
Pd/SSZ-13_900	–	–	–	322	0.16

Fig. 2. ^{27}Al ss-NMR for the 750 °C and 900 °C aged Pd/LTA (black lines) and Pd/SSZ-13 (red lines) samples.

3.1.2. The state of Pd from image results (TEM, HAADF-STEM, and APT)

A combination of TEM and HAADF-STEM imaging techniques were employed to determine the location and dispersion of Pd species in Pd/zeolites before and after aging [29,31]. The M1 and M1' (M = A, and B) images in Fig. 3 show the TEM micrographs of the fresh and 900 °C aged Pd/zeolites, whereas the HAADF-STEM images are shown as M2 and M2' (M = A, and B). By correlating the TEM and HAADF-STEM images for fresh Pd/LTA and Pd/SSZ-13 samples, in combination with in-situ DRIFT (see Section 3.1.4) it is inferred that the majority of Pd atoms were present in the zeolite framework and extra-framework position in the form of ion-exchanged Pd ions (not visible using TEM and HAADF-STEM) and Pd nanoparticles (black dots in TEM and bright dots in HAADF-STEM). The pertinent histograms with particle size distribution were plotted and inserted into the upper left corner of the HAADF-STEM images (A2 and B2) to visualize the distribution of the Pd particle size of fresh samples. Pd nanoparticles in the fresh zeolites clearly showed a very narrow size distribution. Pd nanoparticles mainly had a size of 1 − 2 nm, where the average nanoparticle sizes of 1.6 nm for Pd/LTA_fresh and 1.9 nm for Pd/SSZ-13_fresh were obtained.

A subsequent hydrothermal aging at 900 °C gave rise to the evolution of large Pd particles on the surface of the zeolite in the Pd/SSZ-13_900, suggesting the migration and the resulting sintering of Pd, as shown in B1' and B2'. Only minor amount of Pd particles in the dimension of 1 − 2 nm were observed. But this was not observed for the Pd/LTA sample when aged at 900 °C, as shown in the images in A1' and A2'. Pd remained well dispersed after hydrothermal aging in the Pd/LTA_900 sample. The size of Pd nanoparticles in the Pd/LTA_900 sample was similar to the size of Pd nanoparticles in the Pd/LTA_fresh sample. A main contribution to the difference in the stability of the Pd nanoparticles between Pd/LTA and Pd/SSZ-13 could be due to the diversity in the stability of the zeolite framework structure [20]. Results from BET, XRD, and ^{27}Al ss-NMR (Table 1, Figs. 1, and 2), clearly show that Pd/LTA is more robust compared to Pd/SSZ-13 upon hydrothermal aging, where the physical characteristics of LTA are well maintained, while the framework structure of SSZ-13 is greatly damaged. Therefore,

it was expected that the destruction of the aged Pd/SSZ-13 sample would result in an easier migration and sintering of the Pd species [32–34]. No similar phenomenon was found for the Pd/LTA sample due to its well-maintained zeolite structure. Another study by our group [35] used a Pd/LTA sample with an Si/Al ratio ~ 50 for methane oxidation. That study found that a harsh aging temperature (e.g., 900 °C) caused the severe migration and sintering of Pd species. Generally, zeolite materials with high Si/Al ratio, i.e., less Al content, exhibited better hydrothermal stability, which was widely reported previously. The dealumination of zeolite was considered to be the main reason for structural damage after high-temperature hydrothermal aging. According to the XRD, BET and ^{27}Al-NMR results (Table 1, Figs. 1 and 2), it is clear that the structure of Pd/LTA (Si/Al ~ 15) was largely maintained after 900 °C aging and the phenomenon of dealumination was minimal. Therefore, due to the ultra-high stability of LTA zeolite, under 900 °C hydrothermal aging conditions, the structure stability of Pd/LTA (Si/Al ~ 15) and Pd/LTA (Si/Al ~ 50) did not show much difference. Since the structure of both was not damaged upon 900 °C aging, accordingly, it was suggested that the presence of abundant framework Al sites in Pd/LTA (Si/Al ~ 15) plays a key role in stabilizing Pd species, e.g., PdOx nanoparticles, upon harsh aging. It is most likely that these framework Al sites were the anchors for PdO$_x$ nanoparticles to interact in certain form during the harsh aging, e.g., $[Al-O-Si]^-[PdO_x]^+$.

To further confirm the migration of Pd species for the Pd/SSZ-13 sample when aged, APT analysis was conducted, and reconstructions of the analyses of the Pd/SSZ-13_750 and Pd/SSZ-13_900 samples are presented in Fig. 4. The Pd atoms are illustrated in yellow, indicating a cluster in the Pd/SSZ-13_750 sample (see Supplementary information Fig. S-2 for magnification). The other atoms were evenly distributed. As the Pd is barely visible in the mass spectrum of the Pd/SSZ-13_900 sample, only the possible peak at 106 Da was ranged, and it is shown as Pd in the figures (details shown in Fig. S-3 and Fig. S-4). Thus, many of the atoms shown in the figures are part of the background.

The local composition found using APT is given and listed in Table 2. Although others have reported a low Al content in zeolites analyzed using APT [36,37], the Si/Al ratio measured in the present study was close to what was expected and as measured with other techniques, i.e., ICP shown in Table 1 (Si/Al ~ 15 from ICP and APT). It should be noted that these compositions are local and not representative of the entire zeolite, as the APT analyzed volume was much smaller than a full zeolite particle. The five isotopes of Pd in the Pd/SSZ-13_750 sample can be seen in the mass spectrum (Fig. S-4). There was only one possible indication of Pd after aging at 900 °C, at m/n 106 Da (Fig. S-4). This was the most abundant isotope; the rest may have been obscured by background. Thus, a conservative upper limit of the Pd content was estimated from the ^{106}Pd isotope. The local atomic Pd content was measured to be 0.4 % using APT, which is equal to around ~ 2.0 wt.% in the Pd/SSZ-13_750 sample. This is close to the 1.6 wt.% of Pd measured by ICP for the Pd/SSZ-13 sample (see Table 1). However, less than 0.1 % atomic percentage in the Pd/SSZ-13_900 sample aged at 900 °C was found, which corresponds to less than 0.5 wt.% Pd. It should be noted that before the APT measurements, the sample is sharpened using annular milling to get the correct shape for APT. It is therefore possible that the Pd particles formed on the outside or close to the edges of the zeolite particle during aging is removed during the milling and polishing. Thus, the APT measurements, showing a lower Pd concentration for aged sample, is in line with the TEM and HAADF-STEM images, where it could be observed that most of the Pd species had migrated and sintered on the surface when the Pd/SSZ-13 sample was aged. Moreover, the content of Al was significantly lower after aging at 900 °C, 1.2 at.% as compared to 2.1 at.% after aging at 750 °C, suggesting the occurrence of dealumination, in line with ^{27}Al ss-NMR (Fig. 2).

Radial distribution function (RDF) analysis was also conducted, and the obtained results are displayed in Fig. S-5. PdOx exhibited a Pd-Pd
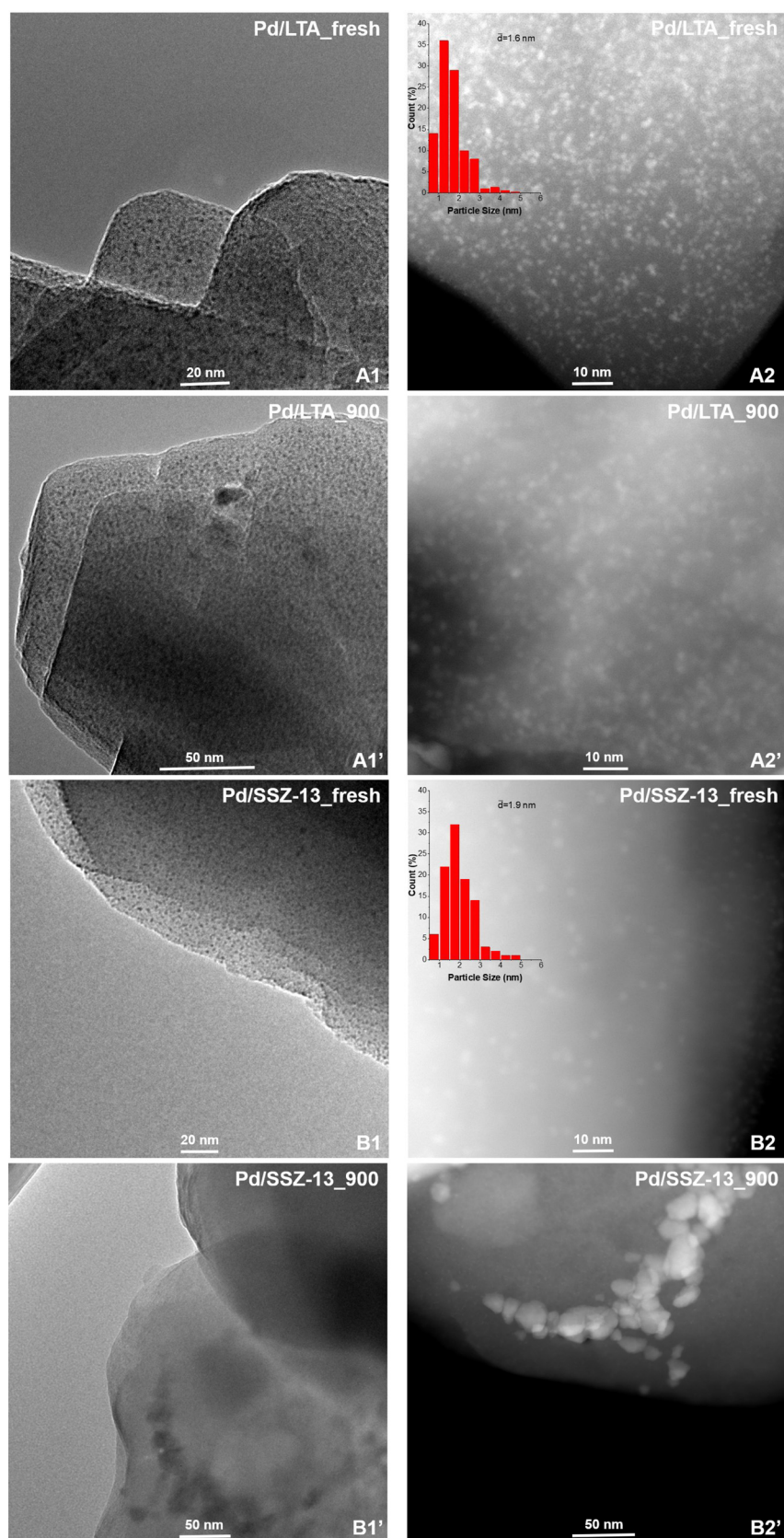
Fig. 3. TEM (left) and HADDF-STEM (right) images for the fresh and 900 °C aged Pd/LTA (A1, A2, A1' and A2') and Pd/SSZ-13 (B1, B2, B1' and B2') samples.
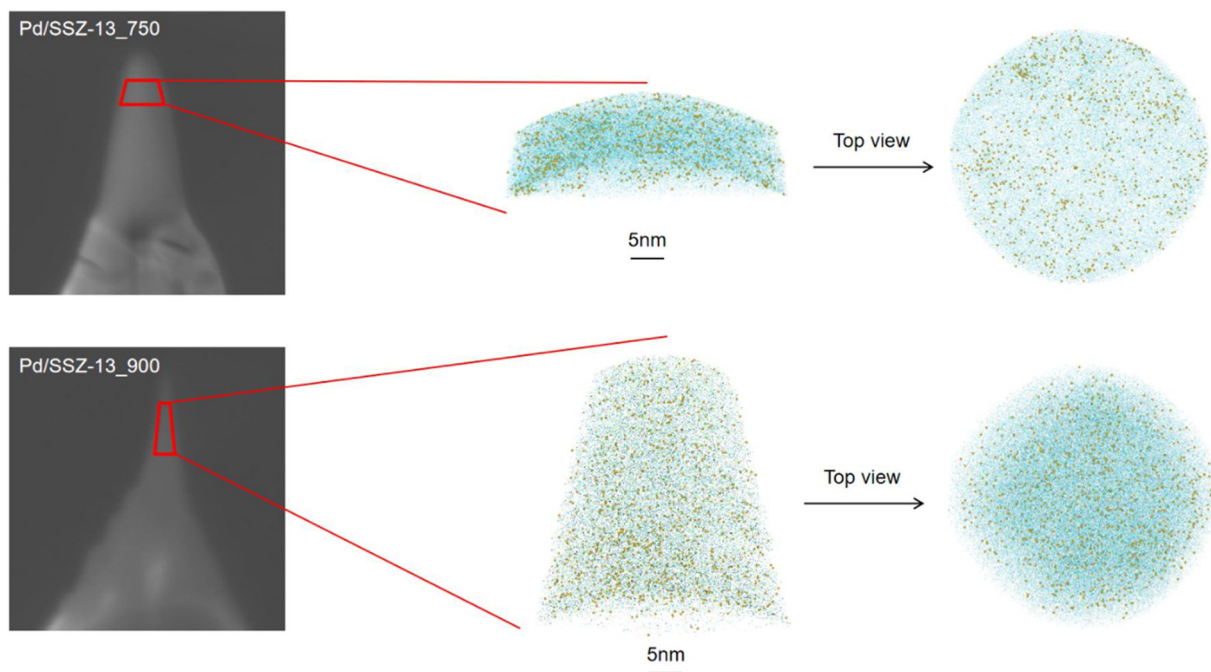
Fig. 4. APT reconstructions. Yellow spheres indicate Pd atoms, blue show the outline of the reconstruction (and correspond to Al, O, and Si). The SEM images of the tips prior to analyses are shown to the left.

Table 2
Local compositions (O, Pd, Al, and Si) from APT analysis.

	Pd/SSZ-13_750		Pd/SSZ-13_900	
	composition (at.%)	error (at.%)	composition (at.%)	error (at.%)
O	63.0	0.29	63.0	0.10
Pd	0.4	0.02	< 0.1	0.03
Al	2.1	0.04	1.2	0.05
Si	34.0	0.19	36.0	0.10

tendency for clustering in the Pd/SSZ-13_750 sample. The Al-Al RDF was unity for all distances in the same material, implying a random distribution of Al atoms. Only the peak at 106 was used for the RDF of Pd-Pd after aging at 900 °C, and there were no indications of clustering

for Pd or Al. It was deduced that only a small amount of monodispersed Pd species was found inside the catalyst after harsh aging at 900 °C for the Pd/SSZ-13 sample.

3.1.3. NH₃ temperature-programmed desorption (NH₃-TPD)

3.1.3. NH_3 temperature-programmed desorption (NH_3-TPD)

Fig. 5 presents the curves from the NH_3-TPD of fresh and aged Pd/LTA and Pd/SSZ-13 samples for an investigation of Lewis and Brønsted acid sites [38,39]. To facilitate the interpretation of the Pd/zeolites, NH_3-TPD experiments were also performed over H/zeolites (gray lines in Fig. 5). Note that NH_3-TPD was performed in the presence of 5 % H_2O. Two predominant NH_3 desorption features were observed for H/LTA and H/SSZ-13 samples: a low-temp shoulder at $150 \sim 200$ °C, assigned to the release of NH_3 from weak acid sites, e.g., external $Si - OH$ and $Al - OH$ [21]; and a high-temp peak at $300 \sim 400$ °C, related to the Brønsted acid sites [40].
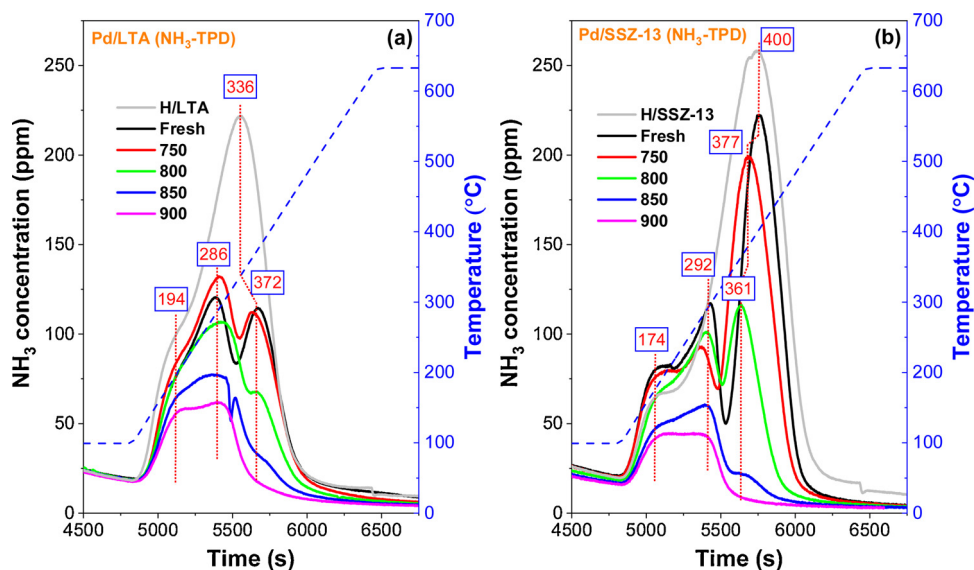

Fig. 5. NH₃-TPD profiles for H/zeolites, fresh and aged Pd/LTA (a) and Pd/SSZ-13 (b) samples.

Investigation of the NH_3-TPD curves for fresh Pd/LTA and Pd/SSZ-13 samples (black lines) showed three distinct desorption peaks, where the newly emerged peak (250~300 °C) was assigned to the stored NH_3 on ion-exchanged Pd sites [41]. Interestingly, more Brønsted sites were used up after the loading of Pd on LTA than on SSZ-13, where the ammonia storage was decreased by 41 % for Pd/LTA, while only by 22 % for Pd/SSZ-13. This phenomenon possibly comes from two reasons: (i) more Pd ion-exchanged with Brønsted acid sites in the LTA zeolite framework. However, this was ruled out based on the NO-TPD profiles shown in Section 3.2.2; (ii) ion-exchanged Pd species (i.e., Pd^{2+} and $[Pd(OH)]^+$) differed between the two zeolites, where Pd^{2+} consumed two nearby Al, and only one Al needed for $[Pd(OH)]^+$. In our previous work [21] with analogous Si/Al ratios and also Cu loadings, the concentration of Cu^{2+} in Cu/LTA was found to be significantly higher than in Cu/SSZ-13, indicating that more Al sites in the framework of LTA are situated in pairs. This will be further discussed in Section 3.1.4 in combination with the NO-DRIFTS results.

Minor changes were found in the Pd/LTA and Pd/SSZ-13 samples upon degreening at 750 °C for 2 h (red lines). The desorption of NH_3 from the Brønsted acid sites decreased significantly when the aging temperature was increased to 800 °C. Meanwhile, no apparent changes were found for the NH_3 desorbed from weak acid sites and isolated Pd sites. These results illustrate that the Pd cationic ions exchanged to the framework are quite robust, while Brønsted acid sites begin to diminish under aging at 800 °C. The NH_3 desorption from both Brønsted acid sites and Pd ions showed a dramatic decrease when the temperature was increased again to 850 °C and then to 900 °C. These results suggest that 850 °C is probably the critical point for Pd ions to detach from the zeolite framework. Brønsted acid sites basically disappeared when the sample was aged at 900 °C. Interestingly, in our previous work [21], the NH_3 storage capacity of Cu/LTA was maintained at remarkable levels after aging at 900 °C. However, the decline was significant for the Pd/LTA sample in the current study. This is probably due to the presence of different Pd species, e.g., PdO_x nanoparticles.

3.1.4. In situ diffuse reflectance infrared fourier transform spectra (DRIFTS)

NO-DRIFTS experiments were conducted on fresh Pd/LTA and Pd/SSZ-13 samples to further characterize Pd species. The IR spectrum after t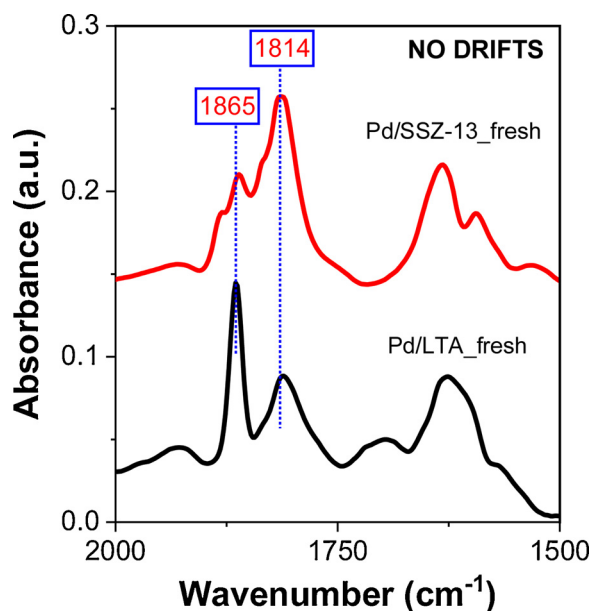he adsorption of NO is shown in Fig. 6. The samples were pretreated with 10 % O_2/Ar for 60 min at 500 °C, and then cooled to 80 °C in the same gas flow prior to NO adsorption. According to the literature, the bands that appear at 1500~1650 cm^{-1} are attributed to the nitrate species [10,42]. This was expected and is consistent with the presence of PdO_x nanoparticles, as seen in the TEM and HAADF-STEM images (Fig. 3), indicating that Pd-nitrate species have been formed. Two nearby bands centered at ~1865 and 1814 cm^{-1} were found in the two samples. The former band, i.e., 1865 cm^{-1}, was attributed to linear nitrosyl species, in which from NO was adsorbed on cationic Pd^{2+}, denoted Pd^{2+}-NO [9,43]. Based on experimental and theoretical data, the assignment of the band at 1814 cm^{-1} was associated with Pd^+-NO [13,43]. Previous studies [13] have proposed the formation mechanism of Pd^+ sites at the adsorption temperature, i.e., 80 °C, according to the following equation:

$$(1)$$

Our experimental data on NO-TPD agrees with this suggestion, where the formation of NO_2 upon the addition of NO was immediately observed.

The key point obtained from NO-DRIFTS is the distinct distribution of these two peaks, at 1865 and 1814 cm^{-1}, between the Pd/LTA and Pd/SSZ-13 samples. The peak at 1865 cm^{-1} was clearly dominant in the Pd/LTA sample and shows that there are more Pd^{2+}-NO [9,43] in Pd/LTA, i.e., more Pd that are bound to two Al. In contrast, 1814 cm^{-1} was the main peak in the Pd/SSZ-13 sample, which indicates more $[Pd(OH)]^+$. This is in consistent with the NH_3-TPD curves (Fig. 5), where more Brønsted acid sites were consumed after the loading of Pd on LTA zeolite, suggesting that more Pd^{2+} species with two nearby framework Al sites were available in the fresh Pd/LTA sample in comparison to the fresh Pd/SSZ-13 sample. This is in line with the Cu/LTA sample as reported in our earlier work [21]. There may be different reasons for the concentration of paired Al sites in LTA zeolite. Recently, Zhang et al. [44] found that the use of different organic templates in the synthesize step would produce different amount of paired Al sites in the CHA zeolite and more paired Al sites resulted in better hydrothermal stability. Therefore, the high concentration of paired Al sites in LTA might be due to the organic template (i.e., 1,2-dimethyl-3-(4-methylbenzyl) imidazolium) used in the synthesis process. At the same time, it is certain that the structure of LTA itself also plays an important role in the distribution of Al.

3.1.5. O_2 temperature-programmed desorption (O_2-TPD)

O_2-TPD experiments was performed from 25 to 800 °C to identify the origin of the difference of the PdO_x species after accelerated temperature-aging Pd/zeolite samples and to reveal the interaction of the bonded oxygen species with the surface of the samples. Fig. 7 presents the O_2-TPD curves of fresh and aged Pd/LTA and Pd/SSZ-13 samples. Note that O_2-TPD was also performed on pure H/LTA and H/SSZ-13 samples (not shown), where no obvious desorption peak of O_2 was found. In the O_2-TPD curves of the Pd/LTA samples, two desorption features are observed: one weak feature located at 110−130 °C, assigned to the desorption of the adsorbed oxygen on the oxygen vacancies on PdO_x species [45]; and a strong feature at 550−650 °C, assigned to the desorption of the lattice oxygen, i.e., the decomposition of PdO_x species [45,46]. Interestingly, only one apparent O_2 desorption peak was found for the Pd/SSZ-13 samples where no obvious surface oxygen species were found to adsorb onto PdO_x species. The results suggest that oxygen vacancies existed in the Pd/LTA samples but not in the Pd/SSZ-13 samples.

The oxygen peak areas originating from the decomposition of PdO_x species can be linked to the oxidation state of Pd and its coordination number [46]. In this context, the decomposition curves of the Pd/zeolites were integrated and normalized to evaluate the amount of O_2 desorption, shown as μmol/$g_{catalyst}$. The values are presented in Table 3. It is a clear trend that the amount of O_2 desorption gradually decreased

Fig. 6. DRIFTS spectra obtained from NO adsorption for fresh Pd/LTA (black line) and fresh Pd/SSZ-13 (red line) samples.
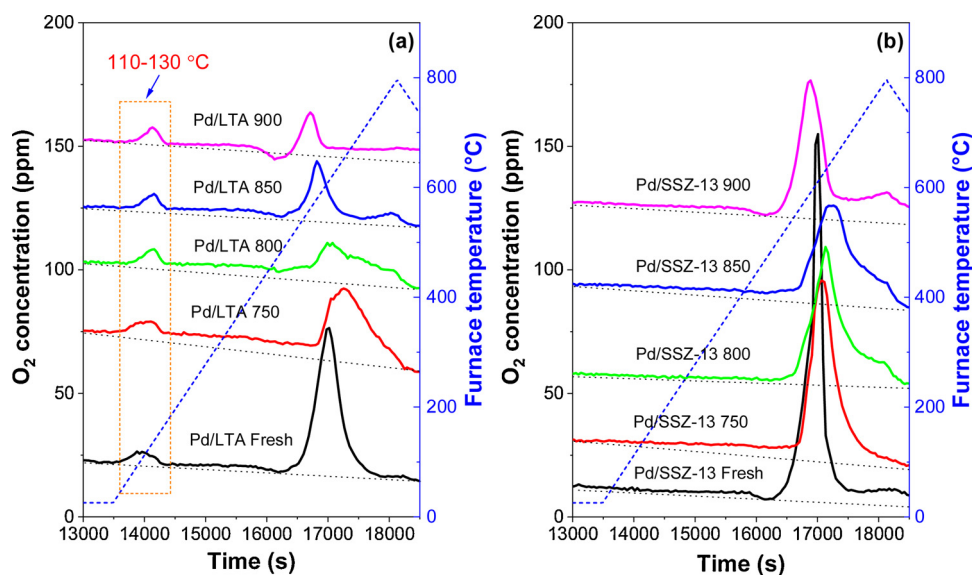
Fig. 7. O$_2$-TPD curves for fresh and aged Pd/LTA (a) and Pd/SSZ-13 (b) samples.

Table 3

O$_2$ desorption amount obtained from O$_2$-TPD profiles for fresh and aged Pd/LTA and Pd/SSZ-13 samples.

Sample	O$_2$ desorption amount (μmol/g$_{catalyst}$)				
	Fresh	750	800	850	900
Pd/LTA	7.9	5.9	3.8	3.1	2.1
Pd/SSZ-13	10.6	9.7	8.7	8.5	7.7

as the aging temperature increased for both Pd/zeolites, which suggests oxidation state and/or oxygen coordination of Pd species decreased. Note that the degree of Pd/LTA decline was significantly higher than that of Pd/SSZ-13 based on Table 3. For example, the desorption amount of O$_2$ decreased from 7.9 to 2.1 μmol/g$_{catalyst}$ (~ 73 %) for the Pd/LTA sample after aging at 900 °C, whereas it only decreased from 10.6–7.7 μmol/g$_{catalyst}$ (~ 27 %) for the Pd/SSZ-13 sample. It is suggested that after aging at 900 °C, most PdO$_x$ nanoparticles in the Pd/LTA sample had been converted to low valence state Pd species, e.g., metallic state, while only a small part in the Pd/SSZ-13 sample was changed. The TEM images (Fig. 3) show that Pd remained well dispersed in the Pd/LTA sample, however, Pd migrated and sintered on the zeolite surface of the Pd/SSZ-13 sample after aging at 900 °C. It can be inferred that bulk PdO$_x$ particles formed in the Pd/SSZ-13 under high

temperature aging maintained a good oxidation capacity.

3.2. Flow reactor

3.2.1. CO oxidation

CO oxidation profiles are presented in Fig. 8a, where 500 ppm CO, 8 % O$_2$, 5 % H$_2$O in Ar with a space velocity of 22 000 h^{-1} was used. The fresh Pd/zeolite samples showed relatively high catalytic activity towards CO oxidation. The catalytic performance of Pd/SSZ-13_fresh was better than Pd/LTA_fresh. For example, the CO conversions at 140 °C were 25 % and 90 % for the Pd/LTA_fresh and the Pd/SSZ-13_fresh samples, respectively. PdO$_x$ nanoparticles are suggested to be highly active for CO oxidation [47]. Therefore, the difference in catalytic activity between these two samples could be due to the following reasons: (1) the quantity of PdO$_x$ nanoparticles, where according to the O$_2$-TPD (Fig. 7 and Table 3), more PdO$_x$ nanoparticles were presented in the Pd/SSZ-13_fresh sample (10.6 μmol/g$_{washcoat}$) than in the Pd/LTA_fresh (7.9 μmol/g$_{washcoat}$) sample; (2) the average sizes of Pd nanoparticles, which were 1.6 nm (Pd/LTA_fresh) and 1.9 nm (Pd/SSZ-13_fresh); and (3) the effect of zeolite supports, i.e., LTA and CHA.

Clearly, as the aging temperature increased, the CO conversion of the two catalysts continuously decreased. To gain better insight into the deactivation between these two samples after aging, the increased T$_{50}$ (ΔT$_{50}$, T$_{50}$ = the temperature of 50 % conversion) was calculated and inserted into the figure. When aged at 900 °C, the obtained ΔT$_{50}$ of Pd/
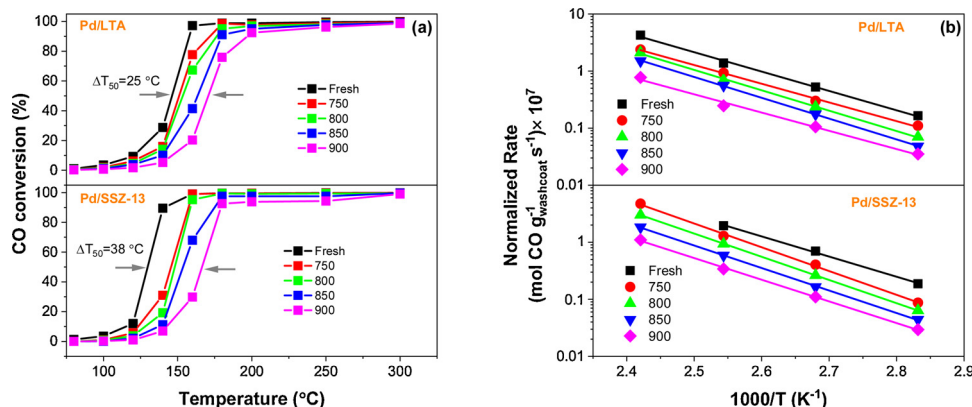

Fig. 8. (a) Conversion versus temperature curves for catalytic CO oxidation in the presence of H$_2$O on the fresh and aged Pd/LTA and Pd/SSZ-13 samples. (b) Arrhenius plots for CO oxidation in the presence of H$_2$O on the fresh and aged Pd/LTA and Pd/SSZ-13 samples.
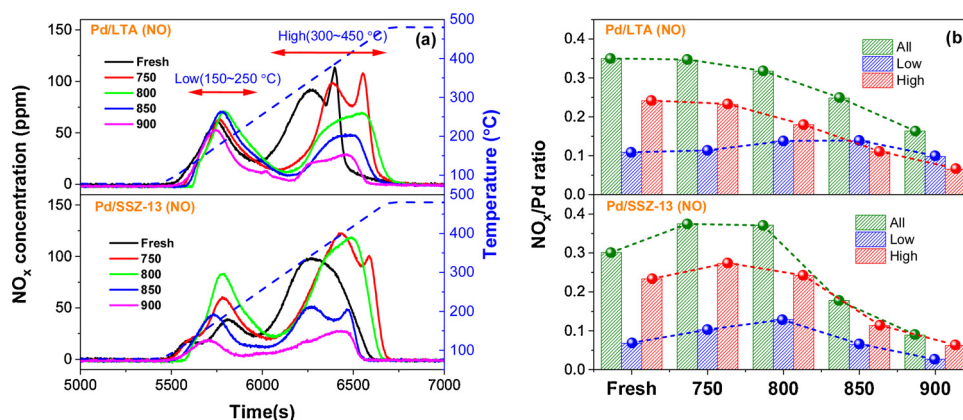
Fig. 9. (a) NO desorption profiles for fresh and aged Pd/LTA and Pd/SSZ-13 samples. NO adsorptions without CO at 80 °C for 60 min. (b) NO_x storage (NO_x/Pd) obtained from NO-TPD profiles for fresh and aged Pd/LTA and Pd/SSZ-13 samples.

LTA and Pd/SSZ-13 were 25 and 38 °C, respectively, as shown in Fig. 8a. It was deduced that the Pd/SSZ-13 sample had undergone more severe deactivation than the Pd/LTA after aging at 900 °C. The key information obtained from the deactivation of Pd/zeolites for CO oxidation upon aging, is that the decrease in valence and the sintering of Pd nanoparticles both affect catalytic activity, where the effect of sintering may be greater.

Fig. 8b shows Arrhenius diagram with the results of low CO conversion normalized to the mass of the washcoat (mol CO $g_{washcoat}^{-1}$ s^{-1}). The apparent activation energies for fresh and aged Pd/LTA and Pd/SSZ-13 samples were similar, ranging from 60 to 80 kJ/mol. An important mechanistic hint can be derived from the close apparent activation energies, i.e., the sites active towards CO oxidation were consistent among all the samples, i.e., PdO_x species [48]. For example, Soni et al. [49] and Kibis and coworkers [50] found that oxidized Pd species (i.e., Pd^{4+}) were significantly active for CO oxidation at low temperature evident from XPS and IR techniques. The corresponding apparent activation energies for all samples are summarized in Fig. S-6 in Supporting Information.

3.2.2. Passive NO_x adsorber (PNA) experiments

Fig. 9(a) displays the NO_x desorption curves in the absence of CO during NO adsorption for fresh and aged Pd/LTA and Pd/SSZ-13 samples. After 60 min of adsorption with 200 ppm NO, the NO concentration remained unchanged, as presented in Fig. S-7 (see Supporting Information), suggesting that the samples had been saturated. Followed by 30 min purge, the catalyst was heated up to 500 °C with the ramp rate of 20 °C/min.

As shown in Fig. 9(a), for fresh Pd/zeolites (black lines), two main

NO_x desorption regions located at low (150 ~ 250 °C) and high (300 ~ 450 °C) temperatures were found, indicating the existence of two distinct forms of NO_x adsorption sites [11]. Fig. 9(b) presents the calculated NO_x/Pd ratios for Pd/LTA sample and Pd/SSZ-13 sample, and the details are listed in Table 4. The ICP results (see Table 1) show that the Pd loading was between 1.4–1.6 wt.%, and it is therefore important to compare the NO_x/Pd ratio and not just the integrated amount [9,43]. One key point is that the aging temperature above 800 °C (i.e. 850 and 900 °C) caused a dramatic decrease in the capacity for NO_x storage for both Pd/zeolite samples, especially for the Pd/SSZ-13. For instance, the NO_x/Pd ratio of the Pd/SSZ-13 sample reached the maximum value of 0.37 after aging at 800 °C, and this dropped to 0.18 after aging at 850 °C, an approximately 52 % drop; however, the decreased storage for Pd/LTA was only ca 22 %, from 0.32 to 0.25.
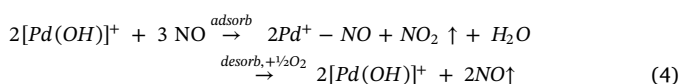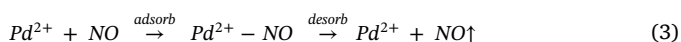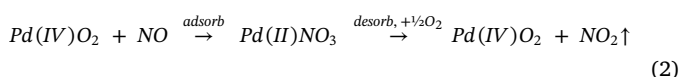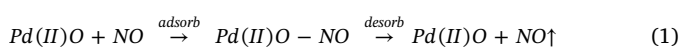
Another interesting point is the evolution trend of the low-temperature desorption amount (150 ~ 250 °C) upon aging. The amount of NO_x desorption at low temperature was well maintained for the Pd/LTA sample (Fig. 9(b), yellow bars). As the aging temperature was increased, the NO_x/Pd ratio increased from 0.11 (fresh) to 0.14 (800 °C), then decreased slightly to 0.10 (900 °C). However, the NO_x/Pd ratio of the Pd/SSZ-13 sample at low temperature increased from 0.07 (fresh) to 0.13 (800 °C) and decreased significantly to 0.03 upon aging at 900 °C. In other words, the NO_x storages decreased slightly from 14.5–13.2 µmol NO_x/$g_{catalyst}$ for Pd/LTA (~ 10 % drop), and from 9.2–3.9 µmol NO_x/$g_{catalyst}$ for Pd/SSZ-13 (~ 60 % drop) at low temperature upon 900 °C aging, suggesting that Pd/SSZ-13 sample experienced a significant loss in NO storage. This will be further discussed later in combination with the assignment of Pd active sites.

According to the literature [10], the majority of the adsorbed NO_x was desorbed at around 300 ~ 400 °C when small-pore zeolites (8MR), e.g., Pd/SSZ-13, were used for the PNA application. This was mainly because the most Pd was at zeolite ion-exchanged sites in the form of Pd^{2+} and $[Pd(OH)]^+$ ions. Lee et al. [11] have systematically studied the different Pd species inside Pd/ZSM-5 sample, where two various Pd sites able to adsorb NO were identified, i.e., PdO_x species and ion-exchanged Pd^{2+}/$[Pd(OH)]^+$ ions. This group has suggested that the NO_x desorption < 300 °C and > 300 °C, can be assigned to PdO_x and Pd^{2+}/$[Pd(OH)]^+$ ions, respectively [11].

The profiles of NO and NO_2 during desorption are displayed in Fig. S-8(a)-(b). NO was the predominant desorption species, where only a low concentration of NO_2 was observed. The curves of NO_2 desorption for all samples are plotted in Fig. S-9 to better understand the evolution of NO_2 desorption with increasing aging temperature. Two main NO_2 desorption peaks can be seen in the figure, one centered at ~ 200 °C and another above 400 °C. The desorption peak above 400 °C could be due to the catalytic oxidation of NO to NO_2 on the PdO_x species [9]. The decrease in NO_2 desorption above 400 °C of the Pd/LTA sample was

Table 4
Capacity for NO_x storage (NO_x/Pd) acquired from NO-TPD experiments for fresh and aged Pd/LTA and Pd/SSZ-13 samples.

Degreening Temperature	CO concentration (ppm)	NO_x/Pd ratio					
		Pd/LTA			Pd/SSZ-13		
		Low	High	All	Low	High	All
Fresh	0	0.11	0.24	0.35	0.07	0.23	0.30
	200	–	–	0.52	–	–	0.41
750	0	0.12	0.23	0.35	0.10	0.27	0.37
	200	–	–	0.55	–	–	0.49
800	0	0.14	0.18	0.32	0.13	0.24	0.37
	200	–	–	0.53	–	–	0.49
850	0	0.14	0.11	0.25	0.06	0.12	0.18
	200	–	–	0.38	–	–	0.24
900	0	0.10	0.06	0.16	0.03	0.06	0.09
	200	–	–	0.20	–	–	0.11

mainly attributed to the decomposition of PdO_x nanoparticles, which was observed during O_2-TPD profiles where less O_2 was desorbing (Fig. 7). For the Pd/SSZ-13 sample it was attributed to the migration and sintering of PdO_x as observed in the STEM images (Fig. 3). This further confirms that PdO_x species are responsible for the NO_2 emitted above 400 °C.

Previous studies have suggested that the NO_2 desorbed below 300 °C is originating from the decomposition of the Pd-nitrates formed [11,15]. In line with their suggestion, extra lattice-oxygen would be required for the formation of Pd-nitrates [11,15]. Our recent work [9] demonstrated that 750 °C aged Pd/SSZ-13 contained relatively higher concentration of Pd^{4+} species than 650 °C aged Pd/SSZ-13 using XPS. A significant increase in NO_2 desorption below 300 °C was observed for the Pd/LTA and Pd/SSZ-13 samples after 750 °C aging (red lines) as presented in Fig. S-9. PdO_2 also satisfied the requirements for the formation of Pd-nitrates, i.e., one extra lattice-oxygen. Therefore, it is natural to link the desorption of NO_2 with the presence of PdO_2. Possible adsorption/desorption approaches can be described as follows:

$$Pd(II)O + NO \xrightarrow{adsorb} Pd(II)O - NO \xrightarrow{desorb} Pd(II)O + NO\uparrow \quad (1)$$

$$Pd(IV)O_2 + NO \xrightarrow{adsorb} Pd(II)NO_3 \xrightarrow{desorb, +\frac{1}{2}O_2} Pd(IV)O_2 + NO_2\uparrow \quad (2)$$

$$Pd^{2+} + NO \xrightarrow{adsorb} Pd^{2+} - NO \xrightarrow{desorb} Pd^{2+} + NO\uparrow \quad (3)$$

$$2[Pd(OH)]^+ + 3\ NO \xrightarrow{adsorb} 2Pd^+ - NO + NO_2 \uparrow + H_2O$$
$$\xrightarrow{desorb, +\frac{1}{2}O_2} 2[Pd(OH)]^+ + 2NO\uparrow \quad (4)$$

$$NO + \frac{1}{2}O_2 \rightleftarrows NO_2\uparrow \quad (5)$$

Reactions (1) and (2) are the possible pathways for the NO/NO_2 desorption below 300 °C, and Reactions (3) - (5) are responsible for NO/NO_2 desorption above 300 °C. To adsorb NO, the PdO_x species (PdO and PdO_2) should be of the size of the nanoparticles [13], which we observe in Figs. 3 and 4 in the TEM and APT images (diameter < 2 nm), or even smaller, e.g., isolated, binuclear, and oligomeric species (not visible in the TEM images) [11,13]. The bulk PdO_x phase has minor NO adsorption capability due to a limited surface area for interaction [11]. Note that the extra oxygen was required in Reaction (2) and (4) during the desorption step to reoxidze the reduced Pd species. The extra oxygen was suggested to origin from adsorption of gas-phase oxygen, considering that 8 % O_2 was maintained in the feed throughout the NO_x adsorption and desorption process.

Pd/SSZ-13 experienced more severe loss of both NO and NO_2 desorption below 300 °C upon aging above 800 °C, as shown in Figs. 9 and S-9. This desorption region (< 300 °C) is mainly attributed to the well-dispersed PdO_x species, e.g., PdO and PdO_2, as discussed above. Due to the severe dealumination of the Pd/SSZ-13 sample and structural damage upon aging above 800 °C, the PdO_x species migrated and sintered on the surface of the zeolite to form larger bulk Pd particles, resulting in a significant loss of NO_x desorption at low temperature. However, this was not found for the Pd/LTA sample, where most Pd nanoparticles remained upon aging as seen by STEM (Fig. 3). The O_2-TPD results suggested a reduction of the valence of Pd nanoparticles in Pd/LTA upon aging (Fig. 7), but no apparent Pd migration according to STEM. Our results show that the NO desorption, at low temperature was maintained after aging of the Pd/LTA. However, it has in earlier studies been found that for severe aging with CO, large metallic Pd particles are formed that are not active for NO adsorption [17,18]. Noted that for the O_2-TPD the pre-treatment with O_2 was done at only 150 °C, and this was probably not enough to reoxidize the decomposed Pd species due to hydrothermal aging, which can explain the low O_2 release in the O_2-TPD for aged Pd/LTA samples. However, the aged catalyst was pretreated at 500 °C using 8 % O_2, 5 % H_2O in Ar and then cooled in the same gas mixture to 80 °C prior to the PNA experiments, and this

pretreatment likely resulted in a re-oxidation of the decomposed Pd species (e.g., reformation of PdO and PdO_2 species), which can explain that the NO/NO_2 release at low temperature was maintained in Pd/LTA after aging.

Fig. 10(a) depicts NO_x desorption curves when 200 ppm CO was added during NO adsorption. The adsorption profiles are shown in Fig. S-10. Clearly, CO had a significant impact on the NO desorption behavior, e.g., storage capacity and desorption temperature. Fig. 10(b) presents the calculated NO_x/Pd ratios for all the samples. In comparison to Fig. 9(b), it is easily found that the presence of CO during NO adsorption can considerably increase the NO_x adsorption ability of Pd/zeolites, regardless of zeolite framework structure [13,16]. For example, the NO_x/Pd ratio of Pd/LTA_750 significantly increased from 0.35 to 0.55 (see Table 4) with the addition of CO, $\sim$ 60 % increase [9]. The increased NO_x storage with CO was proposed to be due to the transformation of Pd(II)-NO species to a mixed carbonyl-nitrosyl complex Pd(II)(NO)(CO), based on experiments with FTIR spectroscopy reported previously [43]. Pd(II)(NO)(CO) species were suggested to be more stable, indicating that the presence of CO increased the storage on some Pd sites that had weak interactions with NO, i.e., no storage at adsorption temperature (80 °C), but with CO, these sites can interact more strongly with NO resulting in increased storage. For a more intuitive understanding, we made a schematic diagram, as shown in Scheme 1 in Supporting Information. Another interesting finding is that a significant reduction of NOx storage was observed in the low temperature region (150 – 250 °C) in the presence of CO. As we discussed above, adsorbed NO_x on PdO_x sites were suggested to be responsible for NO_x desorption at low temperature (150 – 250 °C). Therefore, it is proposed that the presence of CO hindered the formation of Pd(II)O-NO and Pd(II)NO_3 as described in Reaction (1) and (2), and/or directly reduced the PdO_x species. It should be emphasized, however, that the maximum ratios of NO_x/Pd for two samples were much lower than the theoretical value of 1.0, due to the presence of PdO_x. The primary objective of this study was to investigate the effects of hydrothermal aging on different Pd species, not synthesizing a monoatomic dispersion catalyst.

The details of the NO_x/Pd ratios are listed in Table 4, and the increase in the ratios of NO_x storages with the addition of CO were calculated and are presented in Fig. 11. Clearly, the promoted effect of CO on the Pd/LTA sample was considerably higher than on the Pd/SSZ-13 sample. For instance, the NO_x/Pd ratio increased from 0.35 (without CO) to 0.55 (with CO) for the Pd/LTA_750 sample, an approximately 58 % increase, whereas the growth rate for the Pd/SSZ-13_750 sample was ca 30 % (from 0.37 to 0.49). As found in previous work [43], the effect of CO is mainly on the ion-exchanged Pd ions. Thus, this phenomenon is most likely related to the differences in Pd ions (i.e., Pd^{2+} and [Pd(OH)]$^+$) in the two Pd/zeolites. Based on the NH_3-TPD profiles (Fig. 5) and NO-DRIFTS spectra (Fig. 6), Pd^{2+} with two nearby framework Al sites dominated in the fresh Pd/LTA sample, while [Pd(OH)]$^+$ with only one framework Al necessary dominated in the Pd/SSZ-13 sample. Therefore, it was deduced that the improvement of the NO adsorption ability of CO on the Pd^{2+} site is more significant than on the [Pd(OH)]$^+$ site. As presented in Fig. 11, the difference between the Pd/LTA and Pd/SSZ-13 samples due to CO presence, disappeared after aging at 900 °C. We suggest that this is because only a small amount of Pd^{2+} was present in the two samples after aging at 900 °C, which is possible that the Pd^{2+} in Pd/LTA was transformed to [Pd(OH)]$^+$, upon high temperature aging. This is in consistent with our study of Cu/LTA, where we found that Cu^{2+} was transformed to [Cu(OH)]$^+$ during hydrothermal aging [21].

4. Conclusions

Pd/LTA and Pd/SSZ-13 samples, with similar Si/Al ratios and Pd loadings containing multiple Pd species (i.e., isolated Pd ions (Pd^{2+} and [Pd(OH)]$^+$) and 1 ~ 2 nm PdO_x nanoparticles), were synthesized. The
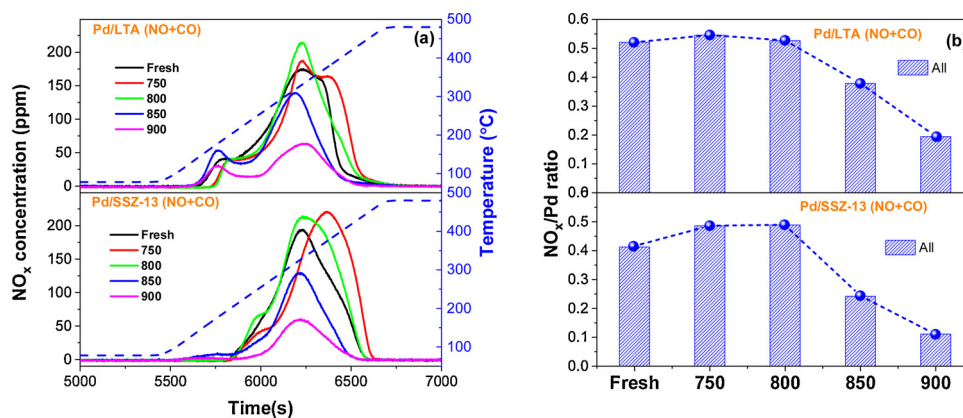
Fig. 10. (a) NO desorption profiles for fresh and aged Pd/LTA and Pd/SSZ-13 samples. NO adsorptions with 200 ppm CO at 80 °C for 60 min. (b) NO$_x$ storage capacity (NO$_x$/Pd) obtained from NO-TPD profiles for fresh and aged Pd/LTA and Pd/SSZ-13 samples.
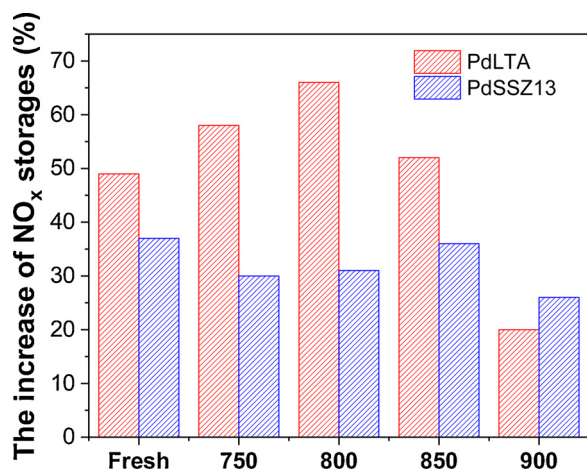

Fig. 11. The increase ratios of NO$_x$ storages with the addition of CO for fresh and aged Pd/LTA and Pd/SSZ-13 samples.

zeolite structure of the Pd/LTA sample was well maintained after harsh aging up to 900 °C, however, the structure of the Pd/SSZ-13 sample experienced severe damage due to dealumination. The destruction of the Pd/SSZ-13 sample upon aging led to the migration and sintering of PdO$_x$ nanoparticles on the zeolite surface to form bulk PdO$_x$ particles. A large number of PdO$_x$ nanoparticles were retained in the aged Pd/LTA sample. It was found that the majority of PdO$_x$ nanoparticles in aged Pd/LTA had converted to low valence state Pd, e.g., the metallic state, which likely were re-oxidized during PNA experiments. However, the bulk PdO$_x$ particles formed in the aged Pd/SSZ-13 sample maintained most of the oxidation state of Pd.

The catalytic activity of Pd/LTA and Pd/SSZ-13 samples for CO oxidation gradually decreased when the aging temperature increased. PdO$_x$ species are proposed to be the active sites for CO oxidation for all samples. It was found that the decrease in the valence and sintering of PdO$_x$ nanoparticles led to a decrease in catalytic activity, where the effect of sintering in the Pd/SSZ-13 sample was greater.

The PNA functionality was examined using NO TPD experiments, and it was found that both Pd/SSZ-13 and Pd/LTA lost significant NO$_x$ storage capacity after hydrothermal aging, but the Pd/LTA had the smallest decrease. For example, after hydrothermal aging at 850 °C, the Pd/SSZ-13 NOx storage dropped 40 % (41 % in presence of CO), while Pd/LTA only decreased with 29 % (27 % in the presence of CO). Moreover, two main NO$_x$ desorption regions located at low (150∼250 °C) and high (300∼450 °C) temperatures were observed in NO-TPD profiles without the addition of CO during adsorption. PdO and PdO$_2$ sites are proposed for NO and NO$_2$ desorption below 300 °C,

respectively. Pd^{2+} and [Pd(OH)]$^+$ ions are responsible for NO desorption above 300 °C, while the NO$_2$ desorption above 300 °C is due to the catalytic oxidation of NO to NO$_2$ by PdO$_x$ species. PdO$_x$ species of the Pd/SSZ-13 sample migrated and sintered on the surface of the zeolite to form bulk Pd particles after aging at 900 °C, resulting in a significant loss of NO$_x$ desorption at low temperature (< 300 °C). However, this was not found for the Pd/LTA sample. Most Pd nanoparticles remained when the sample was aged, which was reflected in the well maintained low-temperature NO$_x$ storage upon 900 °C aging (less than 10 % decrease).

The addition of CO greatly improved the NO$_x$ trapping of the Pd/LTA and Pd/SSZ-13 samples. The CO promoted effect on the Pd/LTA sample was considerably higher compared to the Pd/SSZ-13 sample. It was found that Pd/LTA contained a higher concentration of Pd^{2+} sites, while Pd/SSZ-13 had more [Pd(OH)]$^+$ sites. Therefore, it is deduced that the improvement of NO adsorption ability of CO on Pd^{2+} is more significant than on [Pd(OH)]$^+$.

In addition, the extraordinary thermal stability of Pd nanoparticles (1−2 nm) found in the Pd/LTA sample with Si/Al ∼15 may have potential applications in many other catalytic reactions.

CRediT authorship contribution statement

Aiyong Wang: Conceptualization, Investigation, Writing - original draft. **Kristina Lindgren:** Investigation, Writing - original draft. **Mengqiao Di:** Investigation, Writing - review & editing. **Diana Bernin:** Investigation, Writing - review & editing. **Per-Anders Carlsson:** Supervision, Writing - review & editing. **Mattias Thuvander:** Supervision, Funding acquisition, Writing - review & editing. **Louise Olsson:** Conceptualization, Supervision, Writing - review & editing, Funding acquisition.

Declaration of Competing Interest

The authors declare that they have no known competing financial interests or personal relationships that could have appeared to influence the work reported in this paper.

Appendix A. Supplementary data

Supplementary material related to this article can be found, in the online version, at doi:https://doi.org/10.1016/j.apcatb.2020.119315.

References

[1] E. Borfecchia, P. Beato, S. Svelle, U. Olsbye, C. Lamberti, S. Bordiga, Cu-CHA–a model system for applied selective redox catalysis, Chem. Soc. Rev. 47 (2018) 8097–8133.

[2] P.S. Hammershoi, C. Negri, G. Berlier, S. Bordiga, P. Beat, T.V.W. Janssens, Temperature-programmed reduction with NO as a characterization of active Cu in Cu-CHA catalysts for NH_3-SCR, Catal. Sci. Technol. 9 (2019) 2608–2619.

[3] G. He, Z. Lian, Y. Yu, Y. Yang, K. Liu, X. Shi, Z. Yan, W. Shan, H. He, Polymeric vanadyl species determine the low-temperature activity of V-based catalysts for the SCR of NO_x with NH_3, Sci. Adv. 4 (2018) eaau4637.

[4] Y.T. Gu, W.S. Epling, Passive NO_x adsorber: an overview of catalyst performance and reaction chemistry, Appl. Catal. A-Gen. 570 (2019) 1–14.

[5] Y. Ryou, J. Lee, H. Lee, C.H. Kim, D.H. Kim, Effect of various activation conditions on the low temperature NO adsorption performance of Pd/SSZ-13 passive NO_x adsorber, Catal. Today 320 (2019) 175–180.

[6] Y. Ma, S.Q. Cheng, X.D. Wu, Y.Z. Shi, L. Cao, L.P. Liu, R. Ran, Z.C. Si, J.B. Liu, D. Weng, Low-temperature solid-state ion-exchange method for preparing Cu-SSZ-13 selective catalytic reduction catalyst, ACS Catal. 9 (2019) 6962–6973.

[7] R. Martinez-Franco, M. Moliner, J.R. Thogersen, A. Corma, Efficient one-pot preparation of Cu-SSZ-13 materials using cooperative OSDAs for their catalytic application in the SCR of NO_x, ChemCatChem 5 (2013) 3316–3323.

[8] A. Lundstrom, B. Andersson, L. Olsson, Urea thermolysis studied under flow reactor conditions using DSC and FT-IR, Chem. Eng. J. 150 (2009) 544–550.

[9] A. Wang, K. Xie, A. Kumar, K. Kamasamudram, L. Olsson, Layered Pd/SSZ-13 with Cu/SSZ-13 as PNA − SCR dual-layer monolith catalyst for NO_x abatement, Catal. Today (2020).

[10] H.Y. Chen, J.E. Collier, D.X. Liu, L. Mantarosie, D. Duran-Martin, V. Novak, R.R. Rajaram, D. Thompsett, Low temperature NO storage of zeolite supported Pd for low temperature diesel engine emission control, Catal. Lett. 146 (2016) 1706–1711.

[11] J. Lee, Y. Ryou, S.J. Cho, H. Lee, C.H. Kim, D.H. Kim, Investigation of the active sites and optimum Pd/Al of Pd/ZSM–5 passive NO adsorbers for the cold-start application: evidence of isolated-Pd species obtained after a high-temperature thermal treatment, Appl. Catal. B: Environ. 226 (2018) 71–82.

[12] K. Khivantsev, N.R. Jaegers, L. Kovarik, S. Prodinger, M. Derewisnki, Y. Wang, F. Gao, J. Szanyi, Palladium/beta zeolite passive NOx adsorbers (PNA): clarification of PNA chemistry and the effects of CO and zeolite crystallite size on PNA performance, Appl. Catal. A. Gen. 569 (2018) 141–148.

[13] Y. Zheng, L. Kovarik, M.H. Engelhard, Y.L. Wang, Y. Wang, F. Gao, J. Szanyi, Low-temperature Pd/Zeolite passive NO_x adsorbers: structure, performance, and adsorption chemistry, J. Phys. Chem. C 121 (2017) 15793–15803.

[14] J. Lee, Y. Ryou, S. Hwang, Y. Kim, S.J. Cho, H. Lee, C.H. Kim, D.H. Kim, Comparative study of the mobility of Pd species in SSZ-13 and ZSM-5, and its implication for their activity as passive NO_xadsorbers (PNAs) after hydro-thermal aging, Catal. Sci. Technol. 9 (2019) 163–173.

[15] Y. Ryou, J. Lee, S.J. Cho, H. Lee, C.H. Kim, D.H. Kim, Activation of Pd/SSZ-13 catalyst by hydrothermal aging treatment in passive NO adsorption performance at low temperature for cold start application, Appl. Catal. B-Environ. 212 (2017) 140–149.

[16] K. Khivantsev, N.R. Jaegers, L. Kovarik, S. Prodinger, M.A. Derewinski, Y. Wang, F. Gao, J. Szanyi, Palladium/beta zeolite passive NOx adsorbers (PNA): clarification of PNA chemistry and the effects of CO and zeolite crystallite size on PNA performance, Appl. Catal. A-Gen. 569 (2019) 141–148.

[17] Y. Gu, R.P. Zelinsky, Y.-R. Chen, W.S. Epling, Investigation of an irreversible NO_x storage degradation mode on a Pd/BEA passive NO_x adsorber, Appl. Catal. B: Environ. 258 (2019) 118032.

[18] J. Lee, J.R. Theis, E.A. Kyriakidou, Vehicle emissions trapping materials: successes, challenges, and the path forward, Appl. Catal. B: Environ. 243 (2019) 397–414.

[19] D. Jo, T. Ryu, G.T. Park, P.S. Kim, C.H. Kim, I.S. Nam, S.B. Hong, Synthesis of high-silica LTA and UFI zeolites and NH_3-SCR performance of their copper-exchanged form, ACS Catal. 6 (2016) 2443–2447.

[20] T. Ryu, N.H. Ahn, S. Seo, J. Cho, H. Kim, D. Jo, G.T. Park, P.S. Kim, C.H. Kim, E.L. Bruce, P.A. Wright, I.S. Nam, S.B. Hong, Fully copper-exchanged high-silica LTA zeolites as unrivaled hydrothermally stable NH_3-SCR catalysts, Angew. Chemie Int. Ed. 56 (2017) 3256–3260.

[21] A. Wang, P. Arora, D. Bernin, A. Kumar, K. Kamasamudram, L. Olsson, Investigation of the robust hydrothermal stability of Cu/LTA for NH_3-SCR reaction, Appl. Catal. B: Environ. 246 (2019) 242–253.

[22] J.B. Lim, D. Jo, S.B. Hong, Palladium-exchanged small-pore zeolites with different cage systems as methane combustion catalysts, Appl. Catal. B: Environ. 219 (2017) 155–162.

[23] J.H. Kwak, R.G. Tonkyn, D.H. Kim, J. Szanyi, C.H. Peden, Excellent activity and

[24] selectivity of Cu-SSZ-13 in the selective catalytic reduction of NOx with NH3, J. Catal. 275 (2010) 187–190.

[24] W. Su, Z. Li, Y. Peng, J. Li, Correlation of the changes in the framework and active Cu sites for typical Cu/CHA zeolites (SSZ-13 and SAPO-34) during hydrothermal aging, Phys. Chem. Chem. Phys. 17 (2015) 29142–29149.

[25] Y.-Q. Su, I.A.W. Filot, J.-X. Liu, E.J.M. Hensen, Stable Pd-doped ceria structures for CH_4 activation and CO oxidation, ACS Catal. 8 (2018) 75–80.

[26] A.Y. Wang, Y.L. Wang, E.D. Walter, N.M. Washton, Y.L. Guo, G.Z. Lu, C.H.F. Peden, F. Gao, NH_3-SCR on Cu, Fe and Cu plus Fe exchanged beta and SSZ-13 catalysts: hydrothermal aging and propylene poisoning effects, Catal. Today 320 (2019) 91–99.

[27] J.D. Albarracin-Caballero, I. Khurana, J.R. Di Iorio, A.J. Shih, J.E. Schmidt, M. Dusselier, M.E. Davis, A. Yezerets, J.T. Miller, F.H. Ribeiro, R. Gounder, Structural and kinetic changes to small-pore Cu-zeolites after hydrothermal aging treatments and selective catalytic reduction of NO_x with ammonia, React. Chem. Eng. 2 (2017) 168–179.

[28] M.H. Xu, J. Wang, T. Yu, J.Q. Wang, M.Q. Shen, New insight into Cu/SAPO-34 preparation procedure: impact of NH_4-SAPO-34 on the structure and Cu distribution in Cu-SAPO-34 NH_3-SCR catalysts, Appl. Catal. B: Environ. 220 (2018) 161–170.

[29] L. Kovarik, N.M. Washton, R. Kukkadapu, A. Devaraj, A.Y. Wang, Y.L. Wang, J. Szanyi, C.H.F. Peden, F. Gao, Transformation of active sites in Fe/SSZ-13 SCR catalysts during hydrothermal aging: a spectroscopic, microscopic, and kinetics study, ACS Catal. 7 (2017) 2458–2470.

[30] H.W. Zhao, Y.N. Zhao, M.K. Liu, X.H. Li, Y.H. Ma, X. Yong, H. Chen, Y.D. Li, Phosphorus modification to improve the hydrothermal stability of a Cu-SSZ-13 catalyst for selective reduction of NO_x with NH_3, Appl. Catal. B: Environ. 252 (2019) 230–239.

[31] L. Liu, M. Lopez-Haro, C.W. Lopes, C. Li, P. Concepcion, L. Simonelli, J.J. Calvino, A. Corma, Regioselective generation and reactivity control of subnanometric platinum clusters in zeolites for high-temperature catalysis, Nat. Mater. 18 (2019) 866–873.

[32] H. Hosseiniamoli, G. Bryant, E.M. Kennedy, K. Mathisen, D. Nicholson, G. Sankar, A. Setiawan, M. Stockenhuber, Understanding structure-function relationships in zeolite-supported Pd catalysts for oxidation of ventilation air methane, ACS Catal. 8 (2018) 5852–5863.

[33] I. Friberg, N. Sadokhina, L. Olsson, The effect of Si/Al ratio of zeolite supported Pd for complete CH_4 oxidation in the presence of water vapor and SO_2, Appl. Catal. B: Environ. 250 (2019) 117–131.

[34] A.W. Petrov, D. Ferri, O. Krocher, J.A. van Bokhoven, Design of stable palladium-based zeolite catalysts for complete methane oxidation by postsynthesis zeolite modification, ACS Catal. 9 (2019) 2303–2312.

[35] I. Friberg, A. Wang, L. Olsson, Hydrothermal aging of Pd/LTA monolithic catalyst for complete CH_4 oxidation, Catalysts 10 (2020) 517.

[36] J.E. Schmidt, L. Peng, J.D. Poplawsky, B.M. Weckhuysen, Nanoscale chemical imaging of zeolites using atom probe tomography, Angew. Chemie Int. Ed. 57 (2018) 10422–10435.

[37] J.E. Schmidt, J.D. Poplawsky, B. Mazumder, Ö. Attila, D. Fu, D.M. de Winter, F. Meirer, S.R. Bare, B.M. Weckhuysen, Coke formation in a zeolite crystal during the methanol-to-hydrocarbons reaction as studied with atom probe tomography, Angew. Chemie Int. Ed. 55 (2016) 11173–11177.

[38] R. Villamaina, S. Liu, I. Nova, E. Tronconi, M.P. Ruggeri, J. Collier, A. York, D. Thompsett, Speciation of Cu cations in Cu-CHA catalysts for NH_3-SCR: effects of SiO_2/AlO_3 ratio and Cu-loading investigated by transient response methods, ACS Catal. (2019) 8916–8927.

[39] J.Y. Luo, F. Gao, K. Kamasamudram, N. Currier, C.H.F. Peden, A. Yezerets, New insights into Cu/SSZ-13 SCR catalyst acidity. Part I: Nature of acidic sites probed by NH_3 titration, J. Catal. 348 (2017) 291–299.

[40] K. Xie, A. Wang, J. Woo, A. Kumar, K. Kamasamudram, L. Olsson, Deactivation of Cu-SSZ-13 SCR catalysts by vapor-phase phosphorus exposure, Appl. Catal. B: Environ. 256 (2019) 117815.

[41] C. Wang, X. Ma, Q. Ge, H. Xu, A comparative study of PdZSM-5, Pdβ, and PdY in hybrid catalysts for syngas to hydrocarbon conversion, Catal. Sci. Technol. 5 (2015) 1847–1853.

[42] Y.Y. Ji, S.L. Bai, M. Crocker, Al_2O_3-based passive NOx adsorbers for low temperature applications, Appl. Catal. B: Environ. 170 (2015) 283–292.

[43] K. Khivantsev, N.R. Jaegers, L. Kovarik, J.C. Hanson, F. Tao, Y. Tang, X. Zhang, I.Z. Koleva, H.A. Aleksandrov, G.N. Vayssilov, Achieving atomic dispersion of highly loaded transition metals in small-pore zeolite SSZ-13: a new class of high-capacity and high-efficiency low temperature CO and NO_x adsorbers, Angew. Chemie 130 (2018) 16914–16919.

[44] J. Zhang, Y. Shan, L. Zhang, J. Du, H. He, S. Han, C. Lei, S. Wang, W. Fan, Z. Feng, X. Liu, X. Meng, F.-S. Xiao, Importance of controllable Al sites in CHA framework by crystallization pathways for NH_3-SCR reaction, Appl. Catal. B: Environ. 277 (2020) 119193.

[45] W. Wang, F. Yuan, X. Niu, Y. Zhu, Preparation of Pd supported on La(Sr)-Mn-O perovskite by microwave irradiation method and its catalytic performances for the methane combustion, Sci. Rep.-UK 6 (2016) 19511.

[46] Y. Lou, J. Ma, W.D. Hu, Q.G. Dai, L. Wang, W.C. Zhan, Y.L. Guo, X.M. Cao, Y. Guo, P. Hu, G.Z. Lu, Low-temperature methane combustion over Pd/H-ZSM-5: active Pd sites with specific electronic properties modulated by acidic sites of H-ZSM-5, ACS Catal. 6 (2016) 8127–8139.

[47] A.S. Ivanova, E.M. Slavinskaya, R.V. Gulyaev, V.I. Zaikovskii, O.A. Stonkus, I.G. Danilova, L.M. Plyasova, I.A. Polukhina, A.I. Boronin, Metal–support interactions in Pt/Al_2O_3 and Pd/Al_2O_3 catalysts for CO oxidation, Appl. Catal. B: Environ. 97 (2010) 57–71.

[48] K. Murata, D. Kosuge, J. Ohyama, Y. Mahara, Y. Yamamoto, S. Arai, A. Satsuma,

Exploiting metal–Support interactions to tune the redox properties of supported Pd catalysts for methane combustion, ACS Catal. 10 (2020) 1381–1387.

[49] Y. Soni, S. Pradhan, M.K. Bamnia, A.K. Yadav, S.N. Jha, D. Bhattacharyya, T.S. Khan, M.A. Haider, C.P. Vinod, Spectroscopic evidences for the size dependent generation of Pd species responsible for the low temperature CO oxidation activity on Pd-SBA-15 nanocatalyst, Appl. Catal. B: Environ. 272 (2020) 118934.

[50] L.S. Kibis, A.I. Stadnichenko, S.V. Koscheev, V.I. Zaikovskii, A.I. Boronin, Highly oxidized palladium nanoparticles comprising Pd^{4+} species: spectroscopic and structural aspects, thermal stability, and reactivity, J. Phys. Chem. C 116 (2012) 19342–19348.